Necklacelike Pattern of Vortex Bound States

Zhiyong Hou,[1,*] Kailun Chen,[1,*] Wenshan Hong,[2,3,*] Da Wang,[1,*] Wen Duan,[1] Huan Yang,[1,†] Shiliang Li,[2,4,5] Huiqian Luo,[2,5] Qiang-Hua Wang,[1,‡] Tao Xiang,[2,4,6] and Hai-Hu Wen[1,§]

[1]National Laboratory of Solid State Microstructures and Department of Physics, Collaborative Innovation Center of Advanced Microstructures, Nanjing University, Nanjing 210093, China
[2]Beijing National Laboratory for Condensed Matter Physics, Institute of Physics, Chinese Academy of Sciences, Beijing 100190, China
[3]International Center for Quantum Materials, School of Physics, Peking University, Beijing 100871, China
[4]School of Physical Sciences, University of Chinese Academy of Sciences, Beijing 100190 China
[5]Songshan Lake Materials Laboratory, Dongguan, Guangdong 523808, China
[6]Beijing Academy of Quantum Information Sciences, Beijing 100193, China

(Received 25 July 2024; revised 21 October 2024; accepted 20 December 2024; published 7 February 2025)

A vortex is a topological defect in the superconducting condensate when a magnetic field is applied to a type-II superconductor, as elucidated by the Ginzburg-Landau theory. Because of the confinement of the quasiparticles by a vortex, it exhibits a circular-shaped pattern of bound states with discrete energy levels, as predicted by the Caroli–de Gennes–Matricon theory in 1964. Here, however, we report a completely new type of vortex pattern which is necklacelike in an iron-based superconductor $KCa_2Fe_4As_4F_2$. Our theoretical analysis shows that this necklacelike vortex pattern arises primarily from selective off-shell interference between vortex bound states of opposite angular momenta in the presence of rotational symmetry breaking due to disorders. This fascinating effect can be observed in a system with a small Fermi energy and wave vector, conditions fortuitously met in our samples. Our results not only disclose a novel vortex structure, but also unravel a completely new quantum phenomenon in the superconducting condensate.

DOI: 10.1103/PhysRevX.15.011027 Subject Areas: Condensed Matter Physics

I. INTRODUCTION

In a type-II superconductor, vortices with quantized magnetic flux $\Phi_0 = h/2e$ (with h the Planck constant and e the elementary electric charge) are formed when the magnetic field penetrates the superconductor. Bogoliubov quasiparticles (QPs) exist in the circularly symmetric vortex core with a radius of about the coherence length $\xi \approx hv_F/2\pi^2\Delta_0$ with v_F the Fermi velocity and Δ_0 the bulk superconducting gap value. Based on the Ginzburg-Landau theory [1], the superconducting gap Δ is zero at the vortex center. It gradually increases along the radial direction and finally reaches Δ_0. Since the surrounding superconducting region is protected by the energy gap, the vortex core can be considered as a circular quantum well for QPs in a clean superconductor. As a result, vortex bound states (VBSs) or the so-called Caroli–de Gennes–Matricon (CdGM) states are formed [2]. Based on a simplified analytic solution to the Bogoliubov–de Gennes (BdG) equations by assuming a linear radial (r) variation of Δ, it is predicted that the discrete energy levels of the VBSs should appear at $E_\mu \approx \mu\Delta_0^2/E_F$ (the coefficient $\mu = \pm 1/2, \pm 3/2, \pm 5/2, \ldots$) with E_F the Fermi energy [2–4]. In most superconductors, Δ_0 is very small compared to E_F, and, therefore, the energy interval Δ_0^2/E_F between neighboring levels of VBSs is too small to distinguish. However, in some iron-based superconductors, E_F is comparable with Δ_0, making them ideal platforms for detecting the discrete VBSs. The clear observation of discrete VBSs, especially the high-order ones, was achieved in $FeTe_{0.55}Se_{0.45}$ [5,6] and FeSe monolayer [7] by scanning tunneling microscopy or spectroscopy (STM or STS). In these studies, the ratio of the lowest bound state energies is close to the original prediction of 1:3:5. However, this ratio is found to deviate from the widely believed value in $KCa_2Fe_4As_4F_2$ (K12442, $T_c \approx 33.5$ K) [8]; theoretical analysis indicates that the deviation originates from the nonlinear relationship between Δ and r in the extreme quantum limit condition [9–12]. In addition, spatial oscillations of the bound states can be observed in the radial direction of the vortex core [8–10,13,14].

*These authors contributed equally to this work.
†Contact author: huanyang@nju.edu.cn
‡Contact author: qhwang@nju.edu.cn
§Contact author: hhwen@nju.edu.cn

Meanwhile, in some iron-based superconductors with topological nontrivial band structures, Majorana zero mode, as a particular VBS with $\mu = 0$, can be observed in the vortex cores [15–18], which may be used for topological quantum computing. Usually, the vortex core image and VBSs keep the rotational symmetry, showing a round ring shape of continuous intensity of density of states (DOS). An earlier STM/STS study on $2H$-$NbSe_2$ shows that the CdGM states can be influenced by magnetic impurity scattering, forming the asymmetric pattern of the VBSs [19].

Here, we report a new type of VBSs in K12442 with clear oscillations along the angular direction of the ring featuring the DOS, forming a necklacelike vortex pattern. This has never been predicted by any previous theoretical studies. Based on theoretical calculations involving appropriate disorder scattering, we find that this novel phenomenon can be primarily interpreted by the impurity-induced selective interference between CdGM states of opposite angular momenta. The number of peaks in the interference pattern along the ring provides a direct probe of the microscopic quantity, the angular momentum of the CdGM states in the otherwise absence of impurities.

II. RESULTS

A. Observation of the necklacelike vortex pattern

For a superconductor with an isotropic gap, the discrete energy levels of VBSs are schematically shown in Fig. 1(a) based on the calculated results (see Fig. S1 in Supplemental Material [20]). The calculation is based on the exact diagonalization of the BdG Hamiltonians (see Sec. V) in the extreme quantum limit, and the discrete VBSs can be seen at different energies. Figure 1(b) shows the intensity of the DOS at zero bias, which is induced by the thermal broadening of the lowest levels of VBSs. When the energy is not zero, VBSs manifest themselves as continuous rings of the DOS along the angular direction, as shown in Fig. 1(c). As the energy increases, higher levels of VBSs become dominant and the DOS ring expands its radius [Fig. 1(d)]. In addition, there is a spatial oscillation of the DOS along the radial direction with the period of π/k_F [9,13,14], where k_F is the Fermi wave vector, and one can see the secondary rings outside the main DOS rings in Figs. 1(c) and 1(d).

Although K12442 is a multiband superconductor [21], the major contribution to the surface DOS is given by the smallest holelike α pocket near Γ point with $k_F \approx 0.1\pi/a_0$ from our previous work [22]. Discrete VBSs can be observed in the vortex core (Figs. S3 and S4 [20]) because the extreme quantum limit is satisfied [8]. Vortices can be imaged by differential conductance (dI/dV) mapping at different energies under a magnetic field of 2 T [Figs. 1(e)–1(g) and S2 in Supplemental Material [20]]. The lowest VBS ($\mu = \pm 1/2$) peak can be observed at about ± 1.0 meV on the spectrum measured at the vortex center (Fig. S2 [20]), while the higher-order VBS peaks can be observed when moving away from the core center. A full gap feature with $\Delta_0 = 5.2$ meV can be clearly seen when

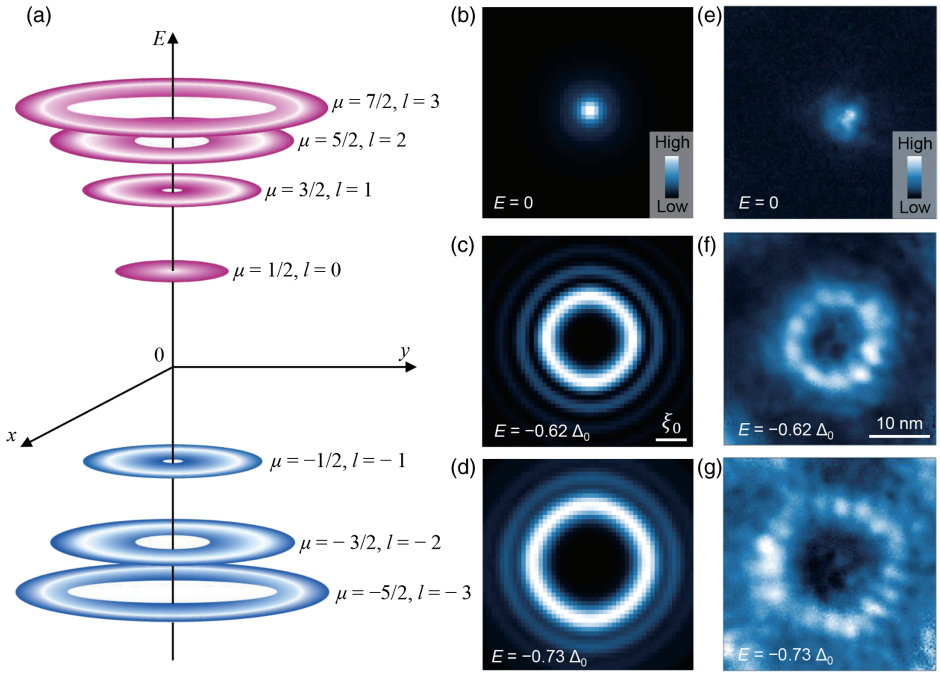

FIG. 1. CdGM states and necklacelike vortex bound states. (a) Schematic diagram of discrete VBS energy levels and the DOS rings based on the calculations of the BdG equations. (b)–(d) Evolution of local DOS of the calculated CdGM states with energy. Δ_0 is the superconducting gap far away from the vortex core, and the parameter $k_F\xi = 5$. (e)–(g) The dI/dV mappings of a necklacelike vortex core measured at different energies inside the superconducting gap in $KCa_2Fe_4As_4F_2$.

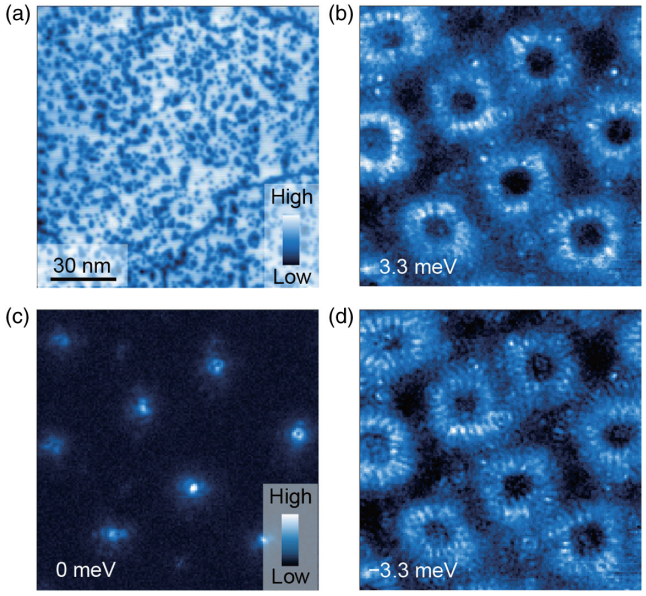

FIG. 2. dI/dV mappings of multiple vortices with necklacelike VBSs in a large area. (a) STM topography of an area in $KCa_2Fe_4As_4F_2$. (b)–(d) dI/dV mappings measured at different energies ($\mu_0 H = 2$ T). The measuring region is the same as (a).

the location is far away from the vortex center, indicating nodeless superconductivity of K12442 [22,23]. Comparing the experimental [Figs. 1(f) and 1(g)] and the calculated [Figs. 1(c) and 1(d)] images of a vortex core at different energies, one can see that the radial variations of DOS show similar behaviors. However, the distribution of DOS along the angular direction appears to strongly deviate from the theoretical result: The calculated DOS exhibits circular rings with uniform and continuous DOS at finite energies below Δ_0, while the measured DOS shows a periodic oscillation in angular direction and the vortex core shows a necklacelike pattern. The oscillation of DOS arising from the VBSs behaves as alternative bright and dark spots along the necklacelike pattern [Figs. 1(f), 1(g), and S2 in Supplemental Material [20]]. The average period of these oscillations is about 3.8 nm, which is close to the value of π/k_F in K12442 [22].

The necklacelike pattern has also been observed in other vortex cores (Figs. S3 and S4 [20]). To further study this novel VBS, we measure the dI/dV mapping in a large area [Figs. 2(a) and S5 in Supplemental Material [20]] to see whether this phenomenon is universal in the system. Under a magnetic field of 2 T, vortices are clearly observed in this area [Figs. 2(b)–2(d)]. However, they do not form a perfect hexagonal lattice, which might be attributed to the vortex pinning effect. In addition, some vortices seem to show a little squarish shape, especially at high energies, which may be due to a slightly fourfold anisotropy of the Fermi velocity and/or the superconducting gap. But this seems to have no influence on the oscillation behavior of DOS on the ring nor the average distance between the neighboring spots (Fig. S5 [20]). It is evident that the necklacelike pattern exists for each vortex and does not depend on the slightly different shape of the vortex.

B. Interference of the VBSs along the angular direction

The angular oscillation behaviors of the VBSs motivate us to consider the interference effect between different CdGM states. For convenience, we use integer quantum number l ($l = \mu - 1/2$) to label the angular momentum of the standard CdGM states:

$$\begin{bmatrix} u_l(\boldsymbol{r}) \\ v_{l+1}(\boldsymbol{r}) \end{bmatrix} = \begin{bmatrix} \psi_l(r)e^{-il\varphi} \\ \psi_{l+1}(r)e^{-i(l+1)\varphi} \end{bmatrix}, \tag{1}$$

with energies $E_l = (l + 1/2)\omega_0$, where $\omega_0 \sim \Delta_0^2/E_F$ and $\psi_l \sim J_l(k_F r)$ for $r \ll \xi$ [2]. Here, J_l is the lth Bessel function of the first kind. The DOS is given by $\rho(\boldsymbol{r}, \omega) = 2\sum_l |u_l|^2 \delta(\omega - E_l)$, where 2 comes from the spin degeneracy. Clearly, the phase information of the CdGM states is lost in the expression of $\rho(\boldsymbol{r}, \omega)$, leaving a continuous circular DOS ring in clean superconductors [Figs. 1(b)–1(d)]. But in the presence of disorders, the rotational symmetry is broken. Few magnetic impurities close to a vortex core can mix the VBSs and induce the asymmetric shape of the vortex core [19], but these sparse impurities cannot lead to the angular oscillation of the VBSs. In the present sample, there are sparse impurities with strong scattering potentials. They can induce an in-gap impurity bound state and behave as bright dots [22], as shown in Fig. 3(a). Besides, there are dense impurities with weak scattering potentials. They cannot induce an apparent in-gap state but act as scattering centers to quasiparticles, forming quasiparticle interference (QPI) patterns [Fig. S2 (i) [20]] at high energies [22]. Note, in the usual QPI picture, the leading effect of the static impurities is the scattering between degenerate extended states [24–26]. Here, the impurities are also expected to mix the VBSs. However, the effect and mechanism are very different. First, the VBSs are nondegenerate, so the elastic scattering between equal-energy states is missing. Second, the mixing of VBSs of different angular momenta is possible only when the impurities break the rotational symmetry. Third, the CdGM states are spatially well separated, with wave function maximum along a ring of radius that is roughly proportional to the (absolute value of the) angular momentum; see Fig. 1(a). The scattering matrix of the impurity potential between two VBSs is, therefore, very restrictive, and the most favorable case is the scattering between VBSs of opposite angular momenta, $\pm l$, that are maximally overlapped.

As such, the interference is between VBSs of unequal energy, an example of the off-shell scattering effect. The effect of such scattering can be captured by the standard nondegenerate perturbation theory. In the first-order approximation, the disorder-corrected CdGM states

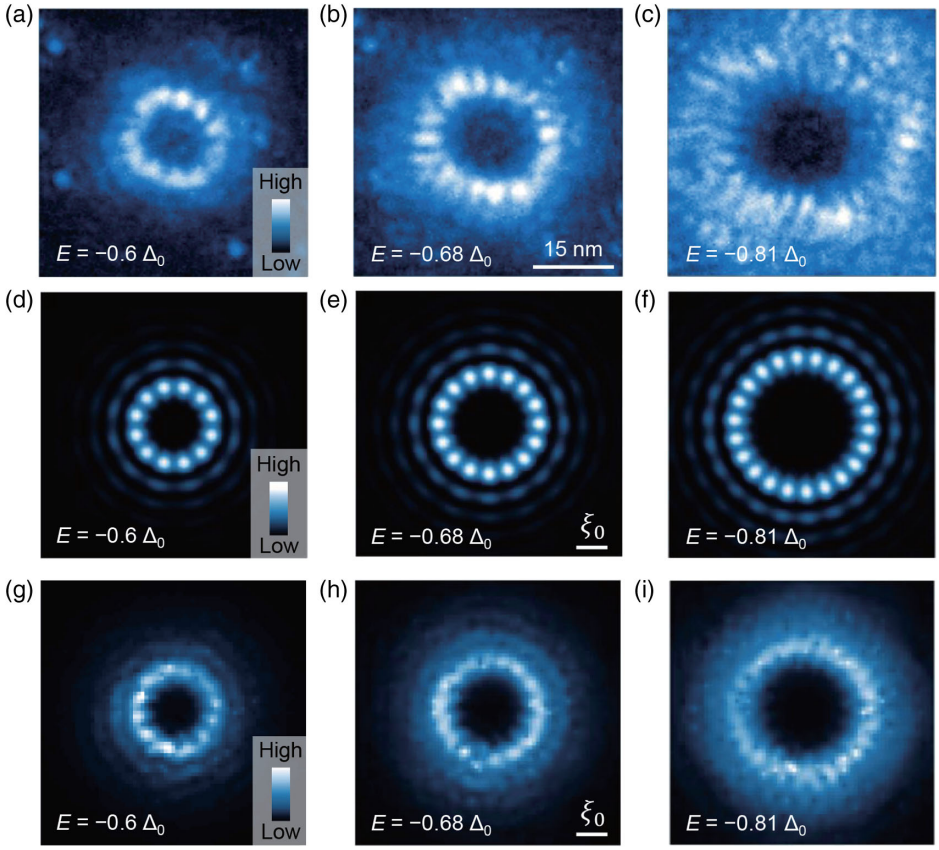

FIG. 3. Isolated vortex core and calculation results by using the disorder-corrected CdGM states. (a)–(c) $\mathrm{d}I/\mathrm{d}V$ mappings of a necklacelike vortex core measured at different energies ($\mu_0 H = 0.2$ T). (d)–(f) Two-level approximation with the parameter $k_F\xi = 5.7$. Here, k_F is set to a similar value as the experimental data, and the theoretical patterns are plotted with the same scale bar as the experimental data. (g)–(i) Numerical calculation results by exact diagonalization of the disorder-corrected CdGM states ($n_{\mathrm{imp}} = 10\%$ of all Fe sites, and $V_{\mathrm{imp}} = 0.36\Delta_0$).

(unnormalized) are given by $\tilde{u}_l = u_l + \sum_{l'} \alpha_{l'l} u_{l'}/(E_l - E_{l'})$ and $\tilde{v}_{l+1} = v_{l+1} + \sum_{l'} \alpha_{l'l} v_{l'+1}/(E_l - E_{l'})$ with the energies $\tilde{E}_l = E_l + \alpha_{ll} + \sum_{l'} |\alpha_{l'l}|^2/(E_l - E_{l'})$. Here, $\alpha_{l'l} = \langle l'|\hat{V}|l\rangle \approx \int (u^*_{l'} V u_l - v^*_{l'+1} V v_{l+1}) \mathrm{d}^2 r$ with V the impurity potential. Therefore, all l'th VBSs other than l have contributions to $\tilde{u}_l$ or $\tilde{v}_{l+1}$. For reasons to become clearer later, we first neglect all other states except $-l$ in order to obtain a minimal model to describe the experimentally observed oscillation behavior. Under this two-level approximation, the resulting local DOS is given by

$$\rho(r,\omega) = 2\sum_l [1 + |\beta_l|^2 + 2|\beta_l| \cos(2l\varphi + \varphi_{0l})]|\psi_l|^2 \times \delta(\omega - \tilde{E}_l), \tag{2}$$

where φ_{0l} is determined by $\beta_l = \alpha_{-l,l}/(E_l - E_{-l})$. In practice, we can use it to simulate the STM data, and β_l is the only fitting parameter, which determines the amplitude and phase of the oscillation. Clearly, there are $2l$ oscillations in the circular direction, and the angular oscillation period is $\Theta_l = 2\pi/2l$. On the other hand, from the radial wave function $\psi_l(r) \sim J_l(k_F r)$, we have an estimation of the radius $R_l \sim l/k_F$, and, thus, the necklace oscillation wave length $\lambda = R_l\Theta_l \sim \pi/k_F$. This provides an essential understanding of the necklace VBSs and demonstrates that the number of peaks in the interference pattern on the ring is directly governed by the important microscopic quantity, the angular momentum of the otherwise unperturbed CdGM states.

C. Fitting results of the experiment data

The two-level approximation [Eq. (2)] allows us to fit the STM data. The radial QP wave functions ψ_l can be calculated by solving the BdG equations (Sec. V). Figures 3(d)–3(f) show the two-level approximation results, which capture the key features of the experimental results. In the above two-level ($\pm l$) analysis, we ignore the correction of the levels $l' \neq -l$. In principle, all states other than $\pm l$ also have contributions to $\tilde{u}_l$ or $\tilde{v}_{l+1}$ which inevitably generate additional harmonics in the wave functions and, thus, complicate the DOS with the oscillation number other than $2l$ (Sec. 1and Figs. S6 and S7 in Supplemental Material [20]). In order to justify or go

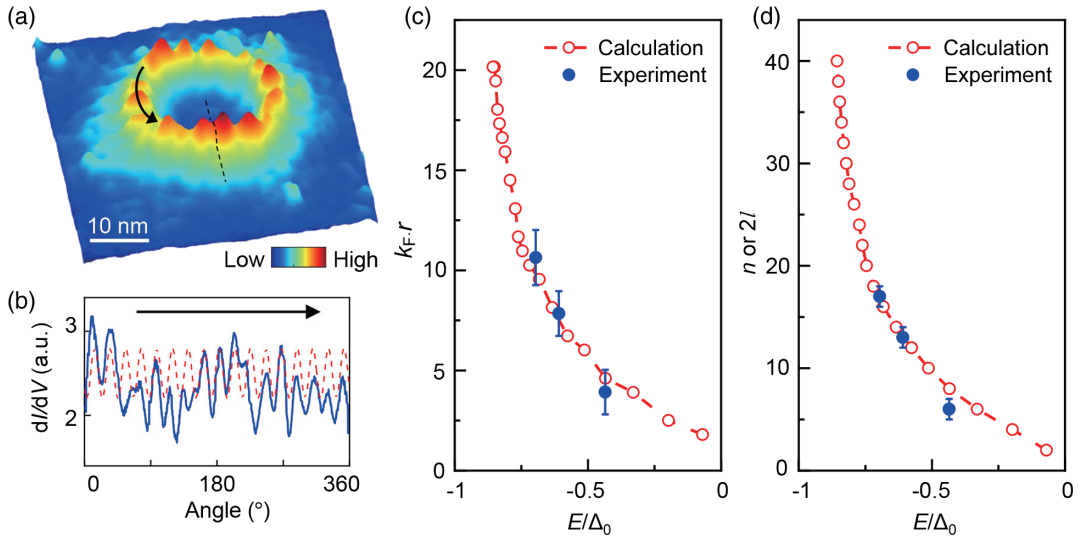

FIG. 4. Comparison of experimental and calculation results. (a) A representative dI/dV mapping of necklacelike VBS pattern plotted in a three-dimensional manner after smoothed. (b) The distribution of dI/dV intensity after smoothing along the DOS ring marked by the black arrow in (a). The initial angle is from the dashed line in (a). The red dashed curve is a sinusoidal function with 17 complete oscillations in a circle. (c) Comparison of the radii of VBS rings acquired from experiment (solid circles) and calculation (empty circles). (d) Comparison of the number of peaks in the DOS ring, i.e., n for experiment (solid circles) and $2l$ for calculation (empty circles). The experimental results consist well with the calculation result with $k_F\xi = 5.7$. The error bars in (c) and (d) are determined by standard errors of the mean values of the radii and the uncertainty in counting the oscillation numbers, respectively.

beyond the two-level approximation, we also perform exact diagonalization calculations on disordered lattices. The numerical results are shown in Figs. 3(g)–3(i). Not only is the radius of the calculated DOS ring consistent with the experimental data, but also the DOS oscillations along the angular direction in the calculation results agree well with the experimental results; even some imperfect oscillation features seen in the experimental data can be simulated. Furthermore, the radiative feature of the spots is also well reproduced. It should be noted that the full-fledged numerical calculations [Figs. 3(g)–3(i)] without assuming any selection rules are consistent with the qualitative picture of selective interference [Figs. 3(d)–3(f)], justifying the qualitative two-level approximation. However, we should emphasize that the two-level approximation is inherently approximate and does not quantitatively agree with the exact diagonalization results or the experimental observations. Its primary purpose is to provide an intuitive framework for interpreting our experimental data. By contrast, the exact diagonalization results offer a more accurate explanation of the experimental observations. At low energies, the radius is too small and the number of spots in the DOS ring is too few, making the oscillation difficult to discern. Nevertheless, it still shows some signs of oscillatory behavior with a similar periodicity. At higher energies near the superconducting gap [Figs. 3(c) and S2 in Supplemental Material [20]], the mixing of the VBSs and the continuum states above the gap cannot give rise to the $2l$ oscillation along the ring but only π/k_F oscillation along random directions, leading to a diffusive feature of DOS. Indeed, the primary and secondary rings smear together at high energies according to the calculation results.

To gain better understanding of our experimental results, we make more quantitative comparisons between the experimental and theoretical results. Through analyzing the local DOS distribution of the necklacelike VBSs, for example, Figs. 3(a)–3(c) and 4(a), we can get the oscillation numbers, namely, n, for each VBS. Along the central line of the primary VBS ring [Fig. 4(a)], the local DOS shows about $n = 17$ complete oscillations [Fig. 4(b)], and this value is close to the oscillation number $2l = 18$ from the calculations [Fig. 3(e)]. Since the radius r of the VBS ring and $2l$ can characterize the VBS pattern along the radial and angular direction, respectively, we plot these values at different energies and show them in Figs. 4(c) and 4(d). The calculation results agree well with the experimental data. This agreement is also observed in several other vortex cores (Figs. S2 and S3 [20]). Therefore, inversely, one can determine the angular momentum l by simply counting the number of peaks ($2l$). In this way, to the best of our knowledge, our work actually measures the angular momenta l of the CdGM states experimentally for the first time. The oscillation period is calculated by $2\pi r/2l$, and the obtained periods are 3.9 ± 0.6, 3.8 ± 0.6, and 4.1 ± 1.3 nm at $E = 0.42\Delta_0$, $0.6\Delta_0$, and $0.68\Delta_0$, respectively. These obtained periods are close to the value of $\pi/k_F \approx 3.9$ nm.

D. Results of the VBSs with variable disorders

In the above, we have learned that the necklace VBSs can be primarily explained by disorder-induced selective

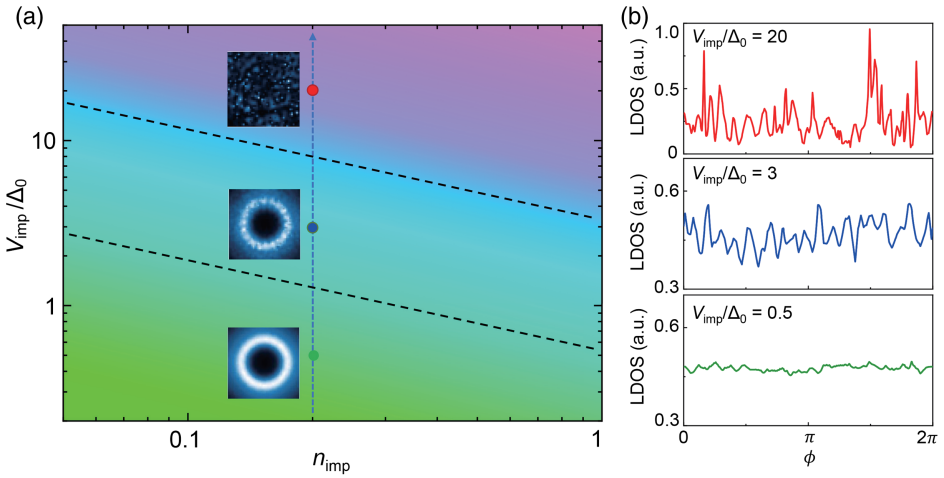

FIG. 5. VBS pattern versus the disorder density and strength. (a) The (n_{imp}, V_{imp}) parameter space contains three regimes: I (ring), II (necklace), and III (featureless). Typical local DOS distributions of the three regimes are shown in the insets. The dark dashed lines show the approximate boundaries between neighbored regimes. (b) Angular distributions of the DOS along the same ring for different V_{imp}. As V_{imp} increases, the curves behave differently from regime I to III.

interference between CdGM states of opposite angular momenta. Next, we investigate the effect of disorder strengths and densities. For disorders of density n_{imp} and scattering potential V_i distributed uniformly in $[-V_{imp}, V_{imp}]$, we can estimate the characteristic scale $\sigma_l = \sqrt{\langle|\alpha_{-l,l}|^2\rangle} \propto \sqrt{\Gamma_{imp}/l}$ by formally averaging over disorder configurations. Here, $\Gamma_{imp} \propto n_{imp}V_{imp}^2$ is the disorder scattering rate. According to Eq. (2), we need Γ_{imp} to be large enough (not in the clean limit) to observe the oscillation behavior. On the other hand, the energy level E_l is also shifted by the disorders. When the shift is much larger than the energy spacing between adjacent CdGM states, the original CdGM states are expected to be destroyed, and, hence, the above analysis will break down. This provides an upper bound of Γ_{imp} (not in the dirty limit) to observe the necklace rings. The above analyses are checked by numerical calculations systematically. The main results are summarized in Fig. 5. The VBS patterns versus n_{imp} and V_{imp} are roughly divided into three regimes, labeled as I, II, and III, respectively [Fig. 5(a)]. Typical local DOS of the three regimes are shown in the insets. With increasing scattering rate Γ_{imp}, the continuous ring (in regime I) is first broken into the necklace shape (in regime II) and finally destroyed (in regime III). From the angular distribution of local DOS along the primary rings [Fig. 5(b)], we can see a transition from regime I to III with increasing Γ_{imp}. More detailed results are shown in Figs. S8 and S9 in Supplemental Material [20]. The results in regime III are well supported by the STM measurements of Ni-doped K12442 samples, where the disorder scattering becomes strong, and the VBSs do not show a well-formed necklace pattern [27]. On the other hand, as discussed above and shown in our calculation (Figs. S10 and S11 [20]), the condition for clearly observing the discrete CdGM states is not the same as that to see the necklace vortex pattern. In the former case, one needs a clean system with a very small disorder scattering rate Γ_{imp}; while in the latter case, an appropriate disorder scattering rate is required. For example, in our previous studies [8], we have seen the discrete CdGM states; meanwhile, in some vortices, we also see the trace of the necklacelike vortex pattern. The occurrences of these two effects are not exclusive to each other but should be dependent on Γ_{imp}.

III. DISCUSSION

Our experiments reveal a new kind of VBS pattern which is necklacelike. Although some vortex patterns look a little squarish at high energies [Figs. 2 and 3(c)], we argue that the necklacelike vortex pattern is not induced by the anisotropy of the superconducting gap or the Fermi velocity. It is clear that the seemingly parallel "sides" of the squarish vortices are approximately along the crystalline axes of the reconstructed surface by K or Ca atoms (the same as the Fe-Fe direction). Some DOS modulation spots in the side regions of the squarish vortex are roughly oriented along two orthogonal directions. However, in the corner regions of the square-shaped vortex, the DOS modulations orient clearly in the diagonal directions showing a radiative feature, which deviates from the above-mentioned two orthogonal directions. Therefore, the spots of DOS modulations show a radiative feature with orientations always perpendicular to the contour of the DOS ring. One may argue that the necklacelike pattern of the VBSs may be caused by the anisotropic superconducting gap or the anisotropic Fermi surface, which can break the rotational symmetry of the vortex core [28,29]. In these cases, vortex cores may exhibit twofold, fourfold, or sixfold

symmetric shapes following the rotational symmetry of Δ_0 or v_F [30–39]. The vortex-core patterns expand in size with increasing energy, but the shape and symmetry do not change clearly [33,34]. Furthermore, this cannot lead to multiple oscillations of DOS with the periodicity of π/k_F along the angular direction. In order to check whether the anisotropy in v_F can induce the oscillation of VBSs along the angular direction, we calculate the VBSs by solving the BdG equations in a clean system with a fourfold symmetric Fermi surface (Fig. S12 [20]), from which one can see the squarish vortex core pattern especially at high energies, but we do not see any signatures of the DOS modulations along the contour of the VBS ring. In addition, from our experiments, we can easily see that the vortex patterns at low energies exhibit a roughly round shape with DOS modulation spots along the radiative direction [Figs. 1(f), 1(g), 3(a), and 3(b)]. This can exclude the possibility that the DOS modulation along the angular direction is induced by the anisotropic Fermi velocity or the gap anisotropy.

As we mentioned above, this exotic pattern of VBSs has been observed in the present iron-based superconducting system with a small Fermi energy E_F or a large Fermi wavelength λ_F, while in the Ni-doped K12442 with a larger residual resistivity (higher disorder density or stronger scattering potential), this phenomenon was not observed [27]. In short, to observe the circular oscillatory VBS rings, we need a small k_F (large λ_F) and an appropriate disorder scattering rate Γ_{imp}, which are not easy to satisfy in most superconductors. However, these conditions are exactly satisfied in some iron-based superconductors, like our present system K12442. Our observation of the novel necklacelike vortex pattern may inspire researchers to see whether such a phenomenon also exists in topological nontrivial vortex with Majorana zero mode and other integer-quantized VBSs, and the recent data seem to show some feature of this [17].

IV. CONCLUSION

In summary, we discovered an unprecedented necklacelike VBS in iron-based superconductor K12442 using STM. In contrast to the continuous DOS ringlike pattern predicted by the BdG equations in the clean limit, here we find a multiple oscillatory feature of VBSs along the angular direction, which has never been observed before and predicted by any previous theoretical studies. The DOS oscillation period is found to be close to π/k_F. In order to interpret the observation, we propose a picture of selective off-shell interference between CdGM states primarily of opposite angular momenta as a result of wave-function matching and rotational symmetry breaking due to disorders. The numerical calculations based on this model reproduce nicely the necklacelike VBSs, which can be most favorably observed in a system with a small Fermi wave vector k_F and appropriate disorder scattering rate Γ_{imp}. This is a significant discovery which provides a new way to detect the angular momenta of the CdGM states experimentally. Our results shed new light on the understanding of the nature of QPs and vortices in superconductors with a small Fermi energy and will stimulate further interest in experimental and theoretical studies.

V. METHOD

A. Sample growth and STM/STS measurements

The K12442 single crystals were grown by the self-flux method [40]. A scanning tunneling microscope (USM-1300, Unisoku Co., Ltd.) was used to carry out the STM/STS measurements. The samples of K12442 were cleaved at about 77 K in an ultrahigh vacuum with a base pressure of about 1×10^{-10} Torr and then transferred to the STM head. Electrochemically etched tungsten tips were cleaned by electron-beam heating and then used for STM/STS measurements. A typical lock-in technique was used in tunneling spectrum measurements with an ac modulation of 0.1 mV and a frequency of 931.773 Hz. Set-point conditions for tunneling spectrum measurements are $V_{set} = 10$ mV and $I_{set} = 200$ pA. All the experimental data were measured at about 0.4 K.

B. Calculations on a lattice model with disorders

We have performed numerical calculations on a square lattice with the Hamiltonian given by

$$H = -t\sum_{\langle ij\rangle\sigma}(c^\dagger_{i\sigma}c_{j\sigma} + \text{H.c.}) + \sum_{i\sigma}(V_i - \mu_c)c^\dagger_{i\sigma}c_{i\sigma} + \sum_i(\Delta_i c^\dagger_{i\uparrow}c^\dagger_{i\downarrow} + \text{H.c.}), \quad (3)$$

where $c^\dagger_{i\sigma}$ creates an electron on site i with spin σ, t is the nearest-neighbor hopping taken as the energy unit, and μ_c is the chemical potential. The pairing function is approximated as $\Delta_i = \Delta_0 \tanh(r_i/\xi)e^{i\phi_i}$, where (r_i, ϕ_i) are polar coordinates of the site i relative to the vortex center. We have added scalar disorder potentials V_i following a uniform distribution $[-V_{imp}, V_{imp}]$ and the density n_{imp} defined as the ratio between the impurity sites and Fe atoms in a layer. By exact diagonalization, the low-energy bound states E_n and (u_n, v_n) are obtained on the $L \times L$ lattice, from which the local DOS is given by

$$\rho(i,\omega) = \frac{2}{\pi}\sum_n \frac{|u_n(i)|^2\eta}{(\omega - E_n)^2 + \eta^2}, \quad (4)$$

where η is the smearing factor. In calculations, unless specified otherwise, we set $\mu_c = -3.5$, $\Delta_0 = 0.1$, $\xi = 10$, $L = 200$, and $\eta = 0.004$. By these parameters, we have $k_F\xi \approx 7$, which is similar to the Γ pocket in K12442.

For $n_{imp} = 0.2$ and $V_{imp} = 3\Delta_0$, we plot the wave functions $|\tilde{u}_l|^2$ with $l = 0, \ldots, 15$ in Fig. S8 [20]. The disorder-induced oscillation can be seen for all the states

except $l = 0$. Of course, for the several low-energy states, since the numbers of necklace oscillations are small, they are easy to be broken by disorder and difficult to identify accurately. On the other hand, for high-energy states, the oscillation is clearly seen and one can always perform Fourier transformation to extract the leading oscillation period. Next, we scan the (n_{imp}, V_{imp}) plane to study the condition to observe the necklacelike behavior. The results of $|\tilde{u}_6|^2$ for a series of (n_{imp}, V_{imp}) are shown in Fig. S9 [20]. Clearly, the complete ring is first broken into the necklace shape and finally destroyed by increasing either n_{imp} or V_{imp}. These results can be roughly understood as explained in the main text: A single parameter $\Gamma_{\mathrm{imp}} \propto n_{\mathrm{imp}} V_{\mathrm{imp}}^2$ can be used to describe the vortex bound states from clean limit (ring) to dirty limit (none), and the necklacelike pattern occurs in between.

ACKNOWLEDGMENTS

We acknowledge helpful discussions with Hong Ding, Christophe Berthod, and Egor Babaev. This work was supported by the National Key R&D Program of China (Grants No. 2022YFA1403200, No. 2018YFA0704200, No. 2023YFA1406100, No. 2022YFA1403400, and No. 2021YFA1400400), National Natural Science Foundation of China (Grants No. 12061131001, No. 11927809, No. 11888101, No. 12374147, and No. 12274205), the Strategic Priority Research Program (B) of the Chinese Academy of Sciences (Grants No. XDB33000000 and No. GJTD-2020-01), and the Youth Innovation Promotion Association of the Chinese Academy of Sciences (Grant No. Y202001).

[1] A. A. Abrikosov, *On the magnetic properties of superconductors of the second group*, Sov. Phys. JETP **5**, 1174 (1957).

[2] C. Caroli, P. G. De Gennes, and J. Matricon, *Bound fermion states on a vortex line in a type II superconductor*, Phys. Lett. **9**, 307 (1964).

[3] L. Kramer and W. Pesch, *Core structure and low-energy spectrum of isolated vortex lines in clean superconductors at* $T \ll T_c$, Z. Phys. **269**, 59 (1974).

[4] T. Xiang and C. Wu, *D-Wave Superconductivity* (Cambridge University Press, Cambridge, England, 2022).

[5] M. Chen, X. Chen, H. Yang, Z. Du, X. Zhu, E. Wang, and H.-H. Wen, *Discrete energy levels of Caroli-de Gennes-Matricon states in quantum limit in* $FeTe_{0.55}Se_{0.45}$, Nat. Commun. **9**, 970 (2018).

[6] L. Kong, S. Zhu, M. Papaj, H. Chen, L. Cao, H. Isobe, Y. Xing, W. Liu, D. Wang, P. Fan, Y. Sun, S. Du, J. Schneeloch, R. Zhong, G. Gu, L. Fu, H.-J. Gao, and H. Ding, *Half-integer level shift of vortex bound states in an iron-based superconductor*, Nat. Phys. **15**, 1181 (2019).

[7] C. Chen, Q. Liu, W.-C. Bao, Y. Yan, Q.-H. Wang, T. Zhang, and D. Feng, *Observation of discrete conventional Caroli-de Gennes-Matricon states in the vortex core of single-layer* $FeSe/SrTiO_3$, Phys. Rev. Lett. **124**, 097001 (2020).

[8] X. Chen, W. Duan, X. Fan, W. Hong, K. Chen, H. Yang, S. Li, H. Luo, and H.-H. Wen, *Friedel oscillations of vortex bound states under extreme quantum limit in* $KCa_2Fe_4As_4F_2$, Phys. Rev. Lett. **126**, 257002 (2021).

[9] N. Hayashi, T. Isoshima, M. Ichioka, and K. Machida, *Low-lying quasiparticle excitations around a vortex core in quantum limit*, Phys. Rev. Lett. **80**, 2921 (1998).

[10] X. Fan, X. Chen, H. Yang, and H.-H. Wen, *Distinct properties of vortex bound states driven by temperature*, Europhys. Lett. **136**, 46002 (2021).

[11] C. Berthod, *Vorticity and vortex-core states in type-II superconductors*, Phys. Rev. B **71**, 134513 (2005).

[12] F. Gygi and M. Schlüter, *Self-consistent electronic structure of a vortex line in a type-II superconductor*, Phys. Rev. B **43**, 7609 (1991).

[13] M. Machida and T. Koyama, *Vortex charge in the superconducting state*, Physica (Amsterdam) **378C–381C**, 443 (2002).

[14] M. Machida and T. Koyama, *Friedel oscillation in charge profile and position dependent screening around a superconducting vortex core*, Phys. Rev. Lett. **90**, 077003 (2003).

[15] D. Wang, L. Kong, P. Fan, H. Chen, S. Zhu, W. Liu, L. Cao, Y. Sun, S. Du, J. Schneeloch, R. Zhong, G. Gu, L. Fu, H. Ding, and H.-J. Gao, *Evidence for Majorana bound states in an iron-based superconductor*, Science **362**, 333 (2018).

[16] Q. Liu, C. Chen, T. Zhang, R. Peng, Y.-J. Yan, C.-H.-P. Wen, X. Lou, Y.-L. Huang, J.-P. Tian, X.-L. Dong, G.-W. Wang, W.-C. Bao, Q.-H. Wang, Z.-P. Yin, Z.-X. Zhao, and D.-L. Feng, *Robust and clean Majorana zero mode in the vortex core of high-temperature superconductor* $(Li_{0.84}Fe_{0.16})OHFeSe$, Phys. Rev. X **8**, 041056 (2018).

[17] W. Liu, L. Cao, S. Zhu, L. Kong, G. Wang, M. Papaj, P. Zhang, Y.-B. Liu, H. Chen, G. Li, F. Yang, T. Kondo, S. Du, G.-H. Cao, S. Shin, L. Fu, Z. Yin, H.-J. Gao, and H. Ding, *A new Majorana platform in an* Fe – As *bilayer superconductor*, Nat. Commun. **11**, 5688 (2020).

[18] M. Li, G. Li, L. Cao, X. Zhou, X. Wang, C. Jin, C.-K. Chiu, S. J. Pennycook, Z. Wang, and H.-J. Gao, *Ordered and tunable Majorana-zero-mode lattice in naturally strained* LiFeAs, Nature (London) **606**, 890 (2022).

[19] S. Park, V. Barrena, S. Mañas-Valero, J. J. Baldovi, A. Fente, E. Herrera, F. Mompeán, M. Garcia-Hernandez, A. Rubio, E. Coronado, A. Levy Yeyati, and H. Suderow, *Coherent coupling between vortex bound states and magnetic impurities in 2D layered superconductors*, Nat. Commun. **12**, 4668 (2021).

[20] See Supplemental Material at http://link.aps.org/supplemental/10.1103/PhysRevX.15.011027 for supporting figures.

[21] D. Wu *et al.*, *Spectroscopic evidence of bilayer splitting and strong interlayer pairing in the superconductor* $KCa_2Fe_4As_4F_2$, Phys. Rev. B **101**, 224508 (2020).

[22] W. Duan, K. Chen, W. Hong, X. Chen, H. Yang, S. Li, H. Luo, and H.-H. Wen, *Single-particle tunneling spectroscopy and superconducting gaps in the layered iron-based superconductor* $KCa_2Fe_4As_4F_2$, Phys. Rev. B **103**, 214518 (2021).

[23] E. Piatti, D. Torsello, G. Ghigo, and D. Daghero, *Spectroscopic studies of the superconducting gap in the 12442 family of iron-based compounds*, Low Temp. Phys. **49**, 770 (2023).

[24] M. F. Crommie, C. P. Lutz, and D. M. Eigler, *Imaging standing waves in a two-dimensional electron gas*, Nature (London) **363**, 524 (1993).

[25] M. F. Crommie, C. P. Lutz, and D. M. Eigler, *Confinement of electrons to quantum corrals on a metal surface*, Science **262**, 218 (1993).

[26] Q.-H. Wang and D.-H. Lee, *Quasiparticle scattering interference in high-temperature superconductors*, Phys. Rev. B **67**, 020511(R) (2003).

[27] W. Duan, K. Chen, W. Hong, X. Chen, S. Li, H. Luo, H. Yang, and H.-H. Wen, *Bamboo-like vortex chains confined in canals with suppressed superconductivity and standing waves of quasiparticles*, Nano Lett. **22**, 9450 (2022).

[28] H. Suderow, I. Guillamón, J. G. Rodrigo, and S. Vieira, *Imaging superconducting vortex cores and lattices with a scanning tunneling microscope*, Supercond. Sci. Technol. **27**, 063001 (2014).

[29] J. E. Hoffman, *Spectroscopic scanning tunneling microscopy insights into* Fe*-based superconductors*, Rep. Prog. Phys. **74**, 124513 (2011).

[30] H. F. Hess, R. B. Robinson, and J. V. Waszczak, *Vortex-core structure observed with a scanning tunneling microscope*, Phys. Rev. Lett. **64**, 2711 (1990).

[31] N. Hayashi, M. Ichioka, and K. Machida, *Star-shaped local density of states around vortices in a type-II superconductor*, Phys. Rev. Lett. **77**, 4074 (1996).

[32] C.-L. Song, Y.-L. Wang, P. Cheng, Y.-P. Jiang, W. Li, T. Zhang, Z. Li, K. He, L. Wang, J.-F. Jia, H.-H. Hung, C. Wu, X. Ma, X. Chen, and Q.-K. Xue, *Direct observation of nodes and twofold symmetry in* FeSe *superconductor*, Science **332**, 1410 (2011).

[33] S.-i. Kaneko, K. Matsuba, M. Hafiz, K. Yamasaki, E. Kakizaki, N. Nishida, H. Takeya, K. Hirata, T. Kawakami, T. Mizushima, and K. Machida, *Quantum limiting behaviors of a vortex core in an anisotropic gap superconductor*, J. Phys. Soc. Jpn. **81**, 063701 (2012).

[34] T. Hanaguri, K. Kitagawa, K. Matsubayashi, Y. Mazaki, Y. Uwatoko, and H. Takagi, *Scanning tunneling microscopy/spectroscopy of vortices in* LiFeAs, Phys. Rev. B **85**, 214505 (2012).

[35] Y. Wang, P. J. Hirschfeld, and I. Vekhter, *Theory of quasiparticle vortex bound states in iron-based superconductors: Application to scanning tunneling spectroscopy of* LiFeAs, Phys. Rev. B **85**, 020506(R) (2012).

[36] Z. Du, D. Fang, Z. Wang, Y. Li, G. Du, H. Yang, X. Zhu, and H.-H. Wen, *Anisotropic superconducting gap and elongated vortices with Caroli-De Gennes-Matricon states in the new superconductor* $Ta_4Pd_3Te_{16}$, Sci. Rep. **5**, 9408 (2015).

[37] M. Chen, X. Chen, H. Yang, Z. Du, and H.-H. Wen, *Superconductivity with twofold symmetry in* $Bi_2Te_3/FeTe_{0.55}Se_{0.45}$ *heterostructures*, Sci. Adv. **4**, eaat1084 (2018).

[38] D. Fang, *Vortex bound states influenced by the Fermi surface anisotropy*, Chin. Phys. B **32**, 037403 (2023).

[39] K. Xiang, D. Wang, and Q.-H.Wang, *Quantized bound states around a vortex in anisotropic superconductors*, Sci. Chin. Phys. Mech. Astron. **67**, 267412 (2024).

[40] T. Wang, J. Chu, H. Jin, J. Feng, L. Wang, Y. Song, C. Zhang, X. Xu, W. Li, Z. Li, T. Hu, D. Jiang, W. Peng, X. Liu, and G. Mu, *Single-crystal growth and extremely high* H_{c2} *of 12442-type Fe-based superconductor* $KCa_2Fe_4As_4F_2$, J. Phys. Chem. C **123**, 13925 (2019).